

**The 3–5 μm Spectrum of NGC 1068 at High Angular Resolution:
Distribution of Emission and Absorption Features across the
Nuclear Continuum Source.**

T. R. Geballe and R. E. Mason

Gemini Observatory, 670 N. A'ohoku Place, Hilo, HI 96720

A. Rodríguez-Ardila

Laboratório Nacional de Astrofísica, Rua dos Estados Unidos 154, Bairro das Nacões, CEP
37500-000, Itajubá, MG, Brazil

D. J. Axon

Department of Physics, Rochester Institute of Technology, 84 Lomb Memorial Drive,
Rochester, NY 14623; and School of Mathematical & Physical Sciences, University of
Sussex, Brighton, East Sussex BN1 9QH, UK

Received _____; accepted _____

ApJ, in press (accepted 2009 June 22)

ABSTRACT

We report moderate resolution 3-5 μm spectroscopy of the nucleus of NGC 1068 obtained at 0.3'' (20 pc) resolution with the spectrograph slit aligned approximately along the ionization cones of the AGN. The deconvolved FWHM of the nuclear continuum source in this direction is 0.3''. Four coronal lines of widely different excitations were detected; the intensity of each peaks near radio knot C, approximately 0.3'' north of the infrared continuum peak, where the radio jet changes direction. Together with the broadened line profiles observed near that location, this suggests that shock-ionization is the dominant excitation mechanism of the coronal lines. The depth of the 3.4 μm hydrocarbon absorption is maximum at and just south of the continuum peak, similar to the 10 μm silicate absorption. That and the similar and rapid variations of the optical depths of both features across the nucleus suggest that substantial portions of both arise in a dusty environment just in front of the continuum source(s). A new and tighter limit is set on the column density of CO. Although clumpy models of the dust screen might explain the shallowness of the silicate feature, the presence of the 3.4 μm feature and the absence of CO are strongly reminiscent of Galactic diffuse cloud environments and a consistent explanation for them and the observed silicate feature is found if all three phenomena occur in such an environment, existing as close as 10 pc to the central engine.

Subject headings: dust, extinction — galaxies: active — galaxies: nuclei — infrared: galaxies — galaxies: individual(NGC 1068)

1. Introduction

The unified model of active galactic nuclei (AGNs) explains the most basic observed properties of AGNs in terms of toroids of dust and gas, whose orientations to our line of sight determine the observed characteristics of these objects. The infrared spectral energy distributions (SEDs) of AGNs betray the presence of dust in their nuclei. Some insight into the properties and distribution of the dust has been gained from observations and modeling of the $9.7\ \mu\text{m}$ silicate feature (Mason et al. 2006; Hönig & Beckert 2007; Roche et al. 2006, 2007) and the $3.4\ \mu\text{m}$ hydrocarbon absorption band (Dartois et al. 2004; Mason et al. 2004, 2007). Notable findings include differences in the spectral profile of the $10\ \mu\text{m}$ silicate feature between galaxies with differing amounts of obscuration (Roche et al. 2007), and evidence that the toroids are rather small, only a few parsecs in diameter at 10 microns (Jaffe et al. 2004; Packham et al. 2005; Poncelet et al. 2006; Tristram et al. 2007; Raban et al. 2009). At shorter wavelengths many AGNs are known to have nuclear point sources, whose angular extents are diffraction-limited (e.g., at $\sim 0.1''$ resolution as viewed in the K -band).

The dust close to an AGN is generally expected to be accompanied by large quantities of molecular gas (Krolik & Begelman 1986), so it might be assumed that medium or high resolution infrared spectroscopy would result in the detection of molecular absorption lines there. Surprisingly, probably the easiest interstellar infrared molecular band to detect in absorption, the CO fundamental ($v=1-0$) band, whose most prominent lines are located at $4.5\text{--}5.0\ \mu\text{m}$, has not yet been found toward the nucleus of the prototypical and nearby (14.4Mpc, $1'' \cong 72\ \text{pc}$; Tully 1988) Seyfert 2 galaxy, NGC 1068, at both $120\ \text{km s}^{-1}$ resolution (Lutz et al. 2004) and at $20\ \text{km s}^{-1}$ resolution (Mason et al. 2006). Line *emission* from molecular hydrogen in portions of the central few parsecs (Müller Sánchez et al. 2009) is the only direct evidence for gas phase molecules there.

A clumpy torus was first suggested by Krolik & Begelman (1988) to account for dust surviving close to AGNs and has been invoked by Nenkova et al. (2002) to explain the behavior of the silicate feature with orientation and the spectral breadth of the far-infrared emission. The model is supported in some specific cases by fits to the SED of an AGN (e.g., Hönig et al. 2008). In NGC 1068 the presence of prominent dust absorption bands both to longer and shorter wavelengths than the CO fundamental band suggest that some CO absorption ought to be present. In Galactic dense cloud material, a silicate optical depth of 0.4, the value found by Mason et al. (2006) toward the nucleus of NGC 1068, implies an H_2 column density of $0.7 \times 10^{22} \text{ cm}^{-2}$ and a CO column density of $1.0 \times 10^{18} \text{ cm}^{-2}$ (Roche & Aitken 1984; Bohlin et al. 1978; Lee et al. 1996), which should be easily detectable in the fundamental band. Toward the diffuse cloud in front of Cyg OB2 No. 12, which has $A_V \sim 10$ mag, the $10 \mu\text{m}$ silicate absorption is of comparable strength to that in NGC 1068 and the $3.4 \mu\text{m}$ absorption band, generally assumed to arise from stretching of C-H bonds in solid-state hydrocarbons (Sandford et al. 1991), is considerably weaker than that band in NGC 1068 (e.g., Whittet et al. 1997; Mason et al. 2004). Nevertheless several (narrow) lines in the CO fundamental band have optical depths of ~ 0.3 (Geballe et al. 1999).

One way for CO to be present but difficult to detect is if the CO lines are so broad that they blend together, so that individual lines cannot be seen. Using different methods Gebhardt et al. (2000) and Bian & Gu (2007) have each estimated the mass of the nuclear black hole in NGC 1068 to be $\sim 2 \times 10^7 M_\odot$. The dimension of the outer of the torus-like clouds observed by Jaffe et al. (2004) and recently re-observed by Raban et al (2009) using mid-infrared interferometry is 2 pc. Together these values imply an orbital speed of 225 km s^{-1} , slightly less than half the spacing of lines in the CO fundamental band. Thus, if absorbing CO is located at the outer edge of the torus, each CO transition would produce an absorption 450 km s^{-1} wide, which is comparable to the CO line spacing. In that case and assuming that the CO rotational states are thermalized to at least a few hundred

Kelvins, the M band spectrum would show a broad and shallow depression covering most of the band and would not be easily detectable in previous data sets. Any CO orbiting considerably farther from the nucleus, however, should be readily detectable in individual lines, if present with sufficient column density. For example, gas orbiting at a radius of 10 pc would produce lines with full widths at zero intensity (FWZIs) of $\sim 200 \text{ km s}^{-1}$.

The high signal-to-noise ratio attainable in the M band for NGC 1068, has allowed us to conduct a new and more sensitive search for CO absorption against the M band continuum at the nucleus of this galaxy. We also have obtained a 3-4 μm spectrum of the nucleus in very good seeing and with high enough S/N to begin to discern the spatial distribution of the 3.4 μm feature within 0.4'' (30 pc) of the nucleus. In the Galaxy this band, due to the C-H stretch in ethyl and methyl groups attached to hydrocarbons, is observed only in diffuse clouds (Pendleton et al. 1994; Chiar et al. 2002). Recent observations of the spatial behavior of the 9.7 μm silicate feature toward AGNs have provided some information on the dust distribution in the central few tens of parsecs (Mason et al. 2006; Rhee & Larkin 2006; Roche et al. 2006, 2007; Young et al. 2007), in several cases revealing extended dusty structures perhaps associated with material fueling the central engine (Packham et al. 2007). Müller Sánchez et al. (2009) have found stronger evidence for fueling of the NGC 1068 AGN, based on high angular resolution observations of H_2 line emission within the central few arc-seconds. More detailed observations of the 3.4 μm band and a more sensitive search for CO absorption promise a complementary view of the material in the center of NGC 1068.

The 3–5 μm region also includes a number of high-excitation forbidden emission lines. Such “coronal” lines in AGNs have been a subject of interest during the last few decades for several reasons. First, their high ionization energies ($>100 \text{ eV}$) imply that they must be excited by shocks and/or hard photons from the AGN, with negligible contribution from

hot stars. If the possible sources of excitation can be disentangled, for example through observation of the locations at which various lines arise, the line strengths and ratios may yield valuable information on the nature of the AGN continuum in otherwise inaccessible regions of the UV/X-ray spectrum. Second, if they are emitted in the inner regions of the narrow line region (NLR), or even associated with the putative torus of the unified model, they can be used indirectly to study those structures. Third, the widths, profiles and wavelength shifts of the lines may map extreme conditions such as shocks and outflows in regions close to the central engine, which may be spatially resolvable in nearby AGNs.

Optical spectroscopy from *Hubble Space Telescope* (HST) has provided detailed information on the morphology of the emission line regions and complex velocity fields of the ionized gas associated with radio structures close to the AGNs (for NGC 1068 see Axon et al. 1998). Although efforts have been made to understand the infrared spectra of AGNs, because of the lack of high spatial resolution information on a well-defined sample, a consensus on the location and origin of the infrared coronal lines has not yet been reached. In this respect, NGC 1068 is a useful laboratory because of the prominent coronal line spectrum that it displays at optical, near-infrared and mid-infrared wavelengths. Whereas the prominent coronal lines in the optical are largely from Fe, the 1.0–2.5 μm region includes several other species, notably Si, Ca and Al, and the 3.0–5.0 μm range includes lines from Al, Si, Ar, and Na.

The new 3–5 μm observations and their reduction are outlined in §2, and the strengths, distributions and profiles of the emission lines and molecular and solid state absorption features are described in §3.2 and §3.3, respectively. Comparisons with previous observations are mostly found in §4. The implications of these findings for our understanding of the environments producing the coronal lines and solid state and possible molecular absorptions are discussed separately in §5.

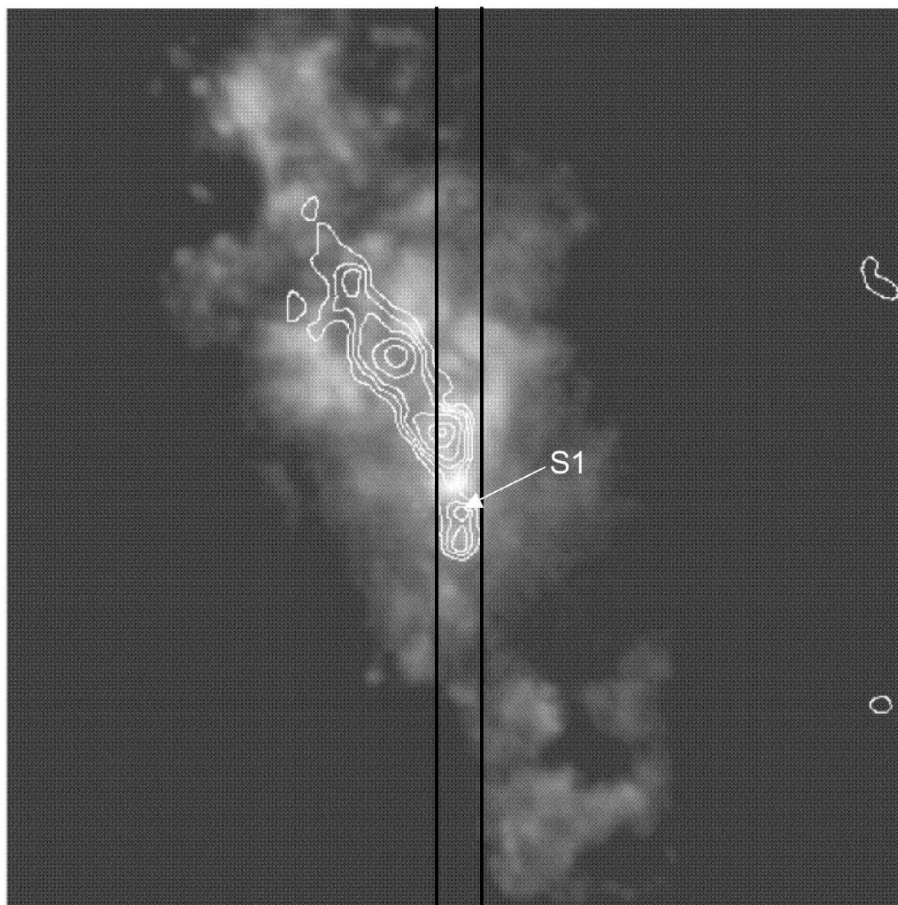


Fig. 1.— Orientation of the $0.2''$ slit used to obtain the $3\text{--}5\ \mu\text{m}$ spectra. North is up and east is to the left. Edges of the slit (vertical lines) are overlayed on Fig. 1 of Capetti et al. (1997), a $4'' \times 4''$ field containing the O III image from Macchetto et al. (1994) and the 6 cm contours of Muxlow et al. (1996). Radio source S1, as designated e.g. in Gallimore et al. (2004), is coincident with the near-infrared continuum peak.

2. Observations and Data Reduction

Spectra of the nuclear region of NGC 1068 and of a nearby calibration star, HR 691 (F0V, L=4.7), were obtained at the United Kingdom Infrared Telescope (UKIRT) on Mauna Kea on 2006 August 10. The facility 1–5 μm imager/spectrograph UIST (Ramsay Howat et al. 2004) was used, with its 0.2'' (2-pixel wide) slit centered on the continuum peak and oriented north-south, as shown in Fig. 1. With that slit width UIST delivers resolving powers, R , of 1400–2400 in various parts of the 3–5 μm region. The orientation roughly corresponds to the position angle of the ionization cones in the central 0.4'' (Gallimore et al. 1996). Rows of the array are separated by 0.10'' along the slit. Table 1 summarizes the observational parameters.

The observations were made in superb seeing conditions and through a photometric and relatively dry sky (1.5 mm of precipitable H_2O). Three spectral regions were covered, 2.9–3.6 μm , 3.6–4.2 μm , and 4.4–5.3 μm . Total exposure times were six minutes in each of the above spectral intervals, and the telescope was nodded 12'' north and back, along the slit in an ABBA pattern which was repeated every two minutes. Long-slit spectra and imaging of H I Br γ at 2.17 μm (Tamura et al. 1991; Davies et al. 1998) have detected no line emission at the offset location.

HR 691 was observed in each spectral interval just prior to NGC 1068 as a flux calibrator and to remove telluric absorption lines from the spectra of NGC 1068 during data reduction. The differences in mean airmass between the pairs of observations of NGC 1068 and calibration star were each one percent or less. The intensity profiles of the continuum from HR 691, measured along the slit have full widths at half maximum (FWHMs) of approximately three pixels 0.3'' (equivalent to 22 pc at the distance of NGC 1068) in all three wavelength bands observed. Assuming that the intensity distribution observed along the slit is circularly symmetric, we estimate that 55 ± 10 percent of the signal from HR 691

fell out of the slit.

Data reduction employed Starlink Figaro routines to extract spectra in individual rows of the UIST detector array from coadditions of several subtracted pairs of images that had been flat-fielded in the UKIRT reduction pipeline. Following manual removal of spikes, spectra from pairs of adjacent rows were combined to produce spectra covering various $0.2'' \times 0.2''$ regions along the slit. These were ratioed by the extracted spectrum of the calibration star. Wavelength calibration, obtained from telluric lines in the spectrum of the calibration star is better than $0.0001 \mu\text{m}$. All wavelength scales in this paper are *in vacuo* and not corrected for the systemic velocity of NGC 1068. The flux calibrations of the reduced $2.9\text{--}3.6 \mu\text{m}$ and $3.5\text{--}4.1 \mu\text{m}$ spectral segments agreed to 3.5 percent in the wavelength interval of overlap, attesting to the excellent weather conditions. Much of the $4.4\text{--}5.4 \mu\text{m}$ region that lies outside of the $4.5\text{--}5.0 \mu\text{m}$ interval is unusable or of little value because of low telluric transmission and is not shown here. In addition, we do not include the reduced spectrum in several narrow wavelength intervals in the $4.80\text{--}5.00 \mu\text{m}$ region, where deep telluric H_2O lines severely degrade the spectra of both the galaxy and the calibration star.

In the $3\text{--}5 \mu\text{m}$ interval the spectrum of the calibration star contains several prominent absorption lines of hydrogen in the Brackett, Pfund, and Humphreys series. Of these only Br α falls in a relatively clean portion of the spectrum and can be removed by interpolation across the observed feature. For the other prominent H I lines we employed a Kurucz R=4,000 model spectrum of Vega with line strengths somewhat diluted in an attempt to match the H I lines of an F0V star. This technique proved successful in removing the Pf β and Hu 11-6 pair at $4.65\text{--}4.67 \mu\text{m}$ but did not work well for simultaneous removal of the Pf γ and Pf δ lines in the short wavelength $2.9\text{--}3.6 \mu\text{m}$ segment. Small wavelength intervals near those lines are omitted in the spectrum presented here.

3. Results

3.1. Dimension of Nuclear Source

Full widths at half maximum (FWHMs) along the slit were determined for both NGC 1068 and the calibration star from the coadded spectral images. The results are shown in Table 1. In all three wavebands the nuclear continuum source in NGC 1068 had a FWHM of approximately four pixels along the slit (compared to three pixels for the calibration star) and was thus partially resolved. A simple Gaussian deconvolution, using the stellar FWHM as the instrumental value yields intrinsic FWHMs for NGC 1068 of $0.27''$ – $0.29''$ in the NS direction (corresponding to a characteristic NS “radius” for the continuum emission of ~ 10 pc). This appears qualitatively consistent with the adaptive optics imaging near these wavelengths by Marco & Alloin (2000) as well as with the more recent and considerably higher resolution imaging of Gratadour et al. (2006). Because the central source is partly resolved in the present data, it is possible to crudely investigate the spatial distribution of the $3.4\ \mu\text{m}$ absorption feature along the slit, in addition to accurately determining the distributions of the emission lines.

3.2. Atomic Lines

Figure 2 shows the 3 – $5\ \mu\text{m}$ spectrum extracted from the central ten rows (i.e., a $0.2'' \times 1.0''$ region of NGC 1068). The expected locations of hydrogen recombination lines and fine structure lines are indicated for a heliocentric systemic radial velocity of $1137\ \text{km s}^{-1}$. In addition to the broad $3.4\ \mu\text{m}$ hydrocarbon feature (Bridger et al. 1994; Imanishi et al. 1997; Mason et al. 2004), four high excitation fine structure (coronal) lines are seen in emission: [Al VI] at $3.660\ \mu\text{m}$, [Si IX] at $3.9357\ \mu\text{m}$, [Ar VI] at $4.5295\ \mu\text{m}$ and [Na VII] at $4.6847\ \mu\text{m}$ (rest wavelengths). Of these the [Al VI] and [Na VII] lines are new detections.

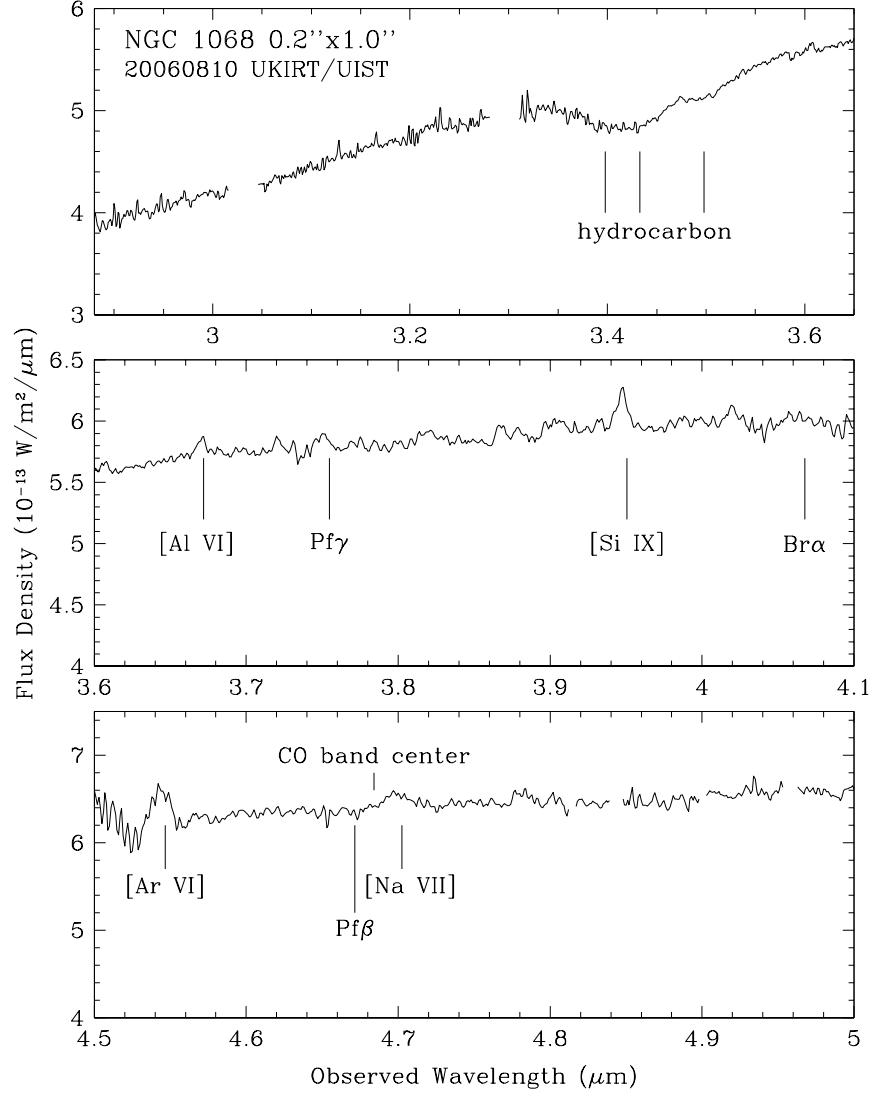


Fig. 2.— Fig. 1: 3–5 μm spectrum of the central $0.2'' \times 1.0''$ (EW x NS) region of NGC 1068. Wavelengths of atomic lines of interest are shown, as are the the three components of the 3.4 μm hydrocarbon feature (Pendleton et al. 1994) and the band center of CO, all at the systemic redshift of 0.003793. The noise level varies but can be estimated at each wavelength from the typical point-to-point fluctuations of the continuum in the vicinity. For simplicity the flux scale assumes that both NGC 1068 and the calibration star are unresolved point sources and that slit losses for them are equal; this is approximately correct for the continuum from NGC 1068, but not for the much more extended line emission.

A tentative detection of the latter was reported by Lutz et al. (2004). The other lines were previously found by Marconi et al. (1996) and Lutz et al. (2000). The coronal lines have FWZIs of over $\sim 1000 \text{ km s}^{-1}$ and the peak of each line is blue-shifted relative to the systemic velocity of NGC 1068 by $\sim 300 \text{ km s}^{-1}$, as has been found previously for other coronal lines in NGC 1068 (Marconi et al. 1996; Lutz et al. 2000; Rodríguez-Ardila et al. 2006). No hydrogen or helium recombination lines are detected in Fig. 2. The marginal emission feature near Pf γ has a profile and a velocity centroid that are inconsistent with all of the other lines, leading us to doubt its reality. There is some marginally significant spectral structure in the vicinity of Br α , near $4.06 \mu\text{m}$, but no obvious sign of line emission.

The coronal line that is detected at the highest signal-to-noise ratio is the [Si IX] line at $3.95 \mu\text{m}$. Si^{+8} has an ionization energy of 303 eV, making it one of the most highly excited species detected in NGC 1068. The next best coronal line for study in these data is the [Al VI] line at $3.67 \mu\text{m}$, which is more than three times weaker, but is situated at shorter wavelengths than other lines and in a region of high atmospheric transmittance so that the ambient background is relatively low and the noise slightly lower than at $3.95 \mu\text{m}$. The ionization energy of Al^{+5} is 154 eV, approximately half that of Si^{+8} . Figure 3 shows both the continuum flux density and the fluxes of these two lines, in $0.2'' \times 0.2''$ apertures along the north-south slit. The line fluxes peak approximately $0.3''$ north of the continuum peak and emission extends northward to $0.8''$. Little or no line emission is present south of the nucleus. The peaks of the line emission from both [Na VII] (ionization energy 172 eV) and [Ar VI] (ionization energy 75 eV) also are offset a few tenths of an arc-second to the north of the continuum peak, similar to [Si IX] and [Al VI], but their detailed distributions are less certain, because of difficulties in accurately removing telluric absorption features and accurately defining the continuum level in the case of the [Ar VI] lines, and because of the weakness of the emission in the case of the [Na VII] line.

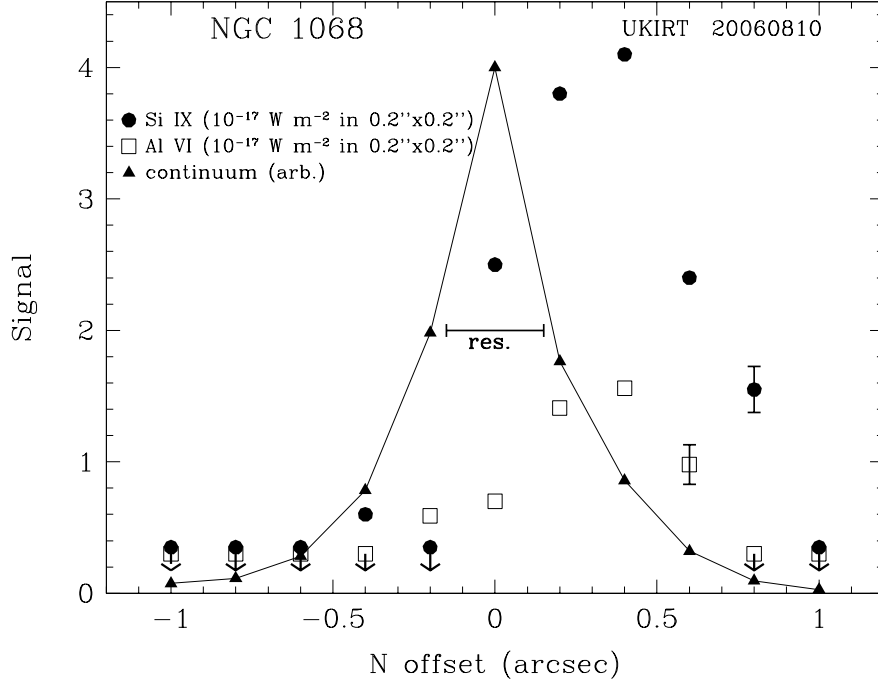


Fig. 3.— Distribution of 3.95 μm continuum, [Si IX], and [Al VI] line flux in 0.2'' sections and 0.2'' steps along the 0.2'' wide slit. Typical $\pm 1\sigma$ uncertainties in line strengths are shown; upper limits, designated by downward arrows, are 2σ . The angular resolution (FWHM = 0.30''), derived from the profile of the standard star, is indicated.

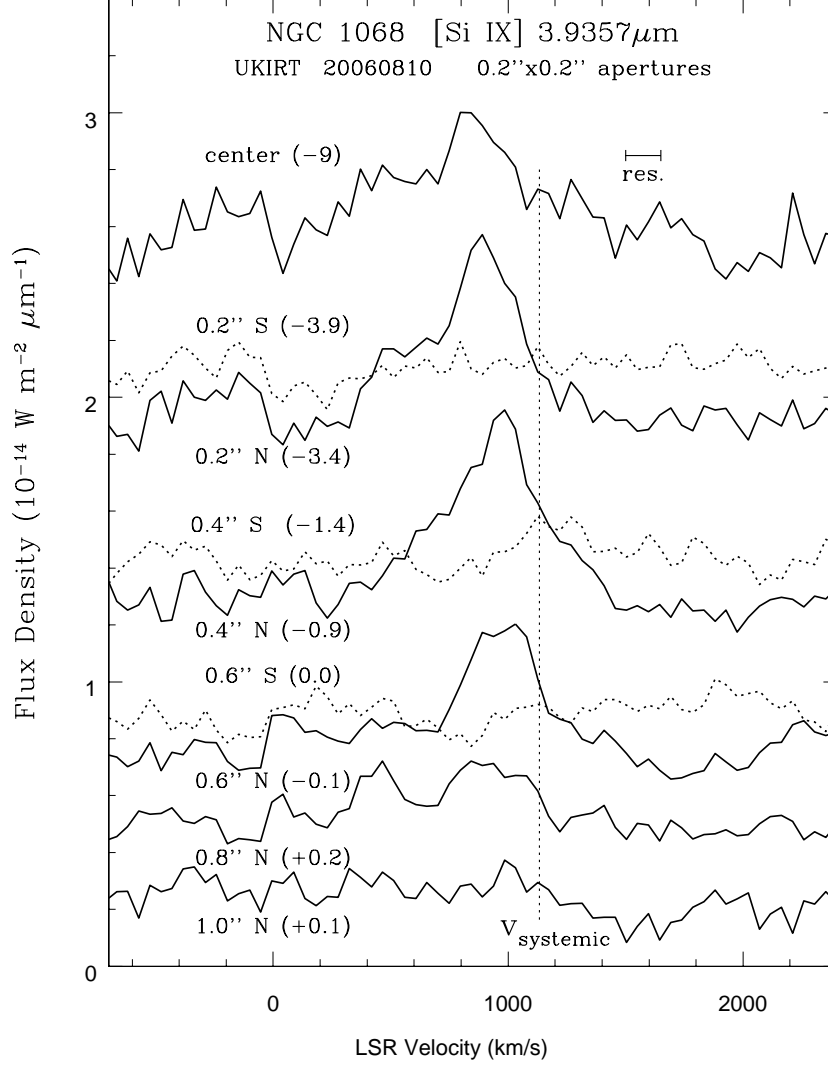


Fig. 4.— Velocity profiles of the [Si IX] line in 0.2'' steps along the slit. Continuous lines denote spectra at the center and to the north; dashed lines indicate spectra to the south. Numbers in parentheses are continuum offsets. The y-axis is flux density in a 0.2'' \times 0.2'' aperture and assumes an estimated slit loss factor of 2.2 for the calibration star. The systemic radial velocity and velocity resolution are shown.

Figure 4 shows the velocity profiles of the [Si IX] line along the north-south slit. The blue-shifted peak seen in the composite spectrum of Fig. 1 is present at all positions from the center to $0.8''$ north. At these locations the velocity of peak line emission is shifted between -200 and -400 km s^{-1} relative to the systemic velocity of NGC 1068. To the south no line emission is seen except perhaps $0.4''$ south where a weak line centered near the systemic velocity may be present. At all of the locations where the line is clearly detected, the velocity profile is asymmetric with an extended blue wing. The wing is most prominent, essentially forming a shoulder, in the central and $0.2''$ north spectra. Overall the line emission appears to extend approximately to -1000 km s^{-1} and $+400 \text{ km s}^{-1}$ from the systemic velocity. This range is similar to that seen in other coronal lines in the $1\text{--}4 \mu\text{m}$ region, e.g., by Lutz et al. (2000).

The line fluxes within the UIST slit given in Table 2 were determined in various ways. Coronal line fluxes derived solely from Fig. 2 will be systematically incorrect because the spectrum has been flux-calibrated using a point source, but the line emission is more extended along the slit than is the continuum. The spectra in Fig. 4 and summed fluxes for the [Si IX] and [Al VI] lines in the table have been corrected for slit losses, using the spectrum of the calibration star. For [Ar VI], and [Na VII], the signal-to-noise ratios are too low to determine fluxes by summing their values at locations along the slit. Therefore we have assumed similar distributions for these lines as [Si IX] and [Al VI]. Then their fluxes in the slit can be estimated by scaling the fluxes derived from Fig. 2 by 0.60, the ratio of the fluxes of the [Si IX] and [Al VI] lines in Table 2 to the values for them derived from Fig. 2. For Br α and Pf γ upper limits were derived solely from the spectrum in Fig. 2.

Table 1. NGC 1068 Observing Log 10 August 2006

Wavelength range	Exp. Time seconds	R $\lambda/\Delta\lambda$	NGC 1068 FWHM ^a arcsec	HR 691 FWHM ^a arcsec
2.9–3.6 μm	360	1400	0.41 ± 0.02	0.31 ± 0.02
3.6–4.2 μm	360	2400	0.42 ± 0.02	0.30 ± 0.03
4.4–5.3 μm	360	2000	0.41 ± 0.03	0.29 ± 0.03

^aMeasured along the slit at 3.4 μm , 3.9 μm , and 4.6 μm .

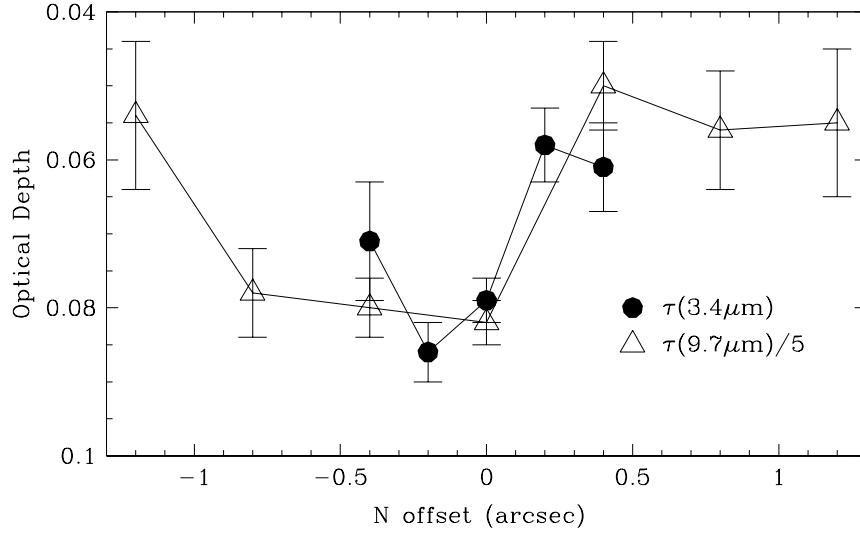


Fig. 5.— Optical depth of the 3.4 μm hydrocarbon absorption feature (this paper) and the 9.7 μm silicate absorption feature (Mason et al. 2006) across the nucleus of NGC 1068. Error bars are $\pm 1\sigma$.

Table 2. NGC 1068 Nuclear Line Fluxes

Line	Ioniz. Energy eV	wavelength rest μm	Flux in Slit ^a $10^{-16} \text{ W m}^{-2}$
[Al VI]	153.8	3.660	0.45 ± 0.10
H I 8-5	13.6	3.7405	< 0.3
[Si IX]	303.2	3.9357	1.5 ± 0.15
H I 5-4	13.6	4.0522	< 0.8
[Ar VI]	75.0	4.5295	2.5 ± 0.7
[Na VII]	172.1	4.6847	1.1 ± 0.3

^aFluxes of coronal lines are derived from Fig. 4 and in the cases of [Ar VI] and [Na VII] by scaling values derived from Fig. 2 as described in the text. The upper limits to the recombination lines are derived from Fig. 2. Upper limits and uncertainties (in parentheses) are 2σ ; uncertainties are mainly due to uncertainty in the continuum level.

3.3. Solid-state and molecular absorptions

The $3.4\ \mu\text{m}$ hydrocarbon absorption feature is the only solid-state feature present in the $3\text{--}5\ \mu\text{m}$ spectrum. It extends from $3.35\ \mu\text{m}$ to perhaps $3.57\ \mu\text{m}$ with a broad absorption maximum near $3.41\ \mu\text{m}$ and a shoulder that begins at $3.47\ \mu\text{m}$. Assuming that the contribution of the $3.43\ \mu\text{m}$ component drops to zero at $3.50\ \mu\text{m}$, the absorption maximum of the shoulder feature occurs close to $3.50\ \mu\text{m}$. After accounting for the redshift of NGC 1068, the above wavelengths and the overall profile are in good agreement with those observed for the $3.4\ \mu\text{m}$ feature in Galactic sources (Pendleton et al. 1994).

The optical depth of the $3.4\ \mu\text{m}$ feature has been determined by fitting a linear continuum across the $3.10\text{--}3.35\ \mu\text{m}$ interval (excluding the $3.29\text{--}3.33\ \mu\text{m}$ region) and the $3.57\text{--}3.60\ \mu\text{m}$ interval. The maximum optical depth of the $3.4\ \mu\text{m}$ feature shown in Fig. 2 is 0.072 ± 0.004 .

Using the same technique we also have measured the optical depth of the $3.4\ \mu\text{m}$ feature in $0.2''$ steps within $\pm 0.4''$ of the infrared continuum peak. The results are shown in Fig. 5, together with the measurements of the optical depth of the $9.7\ \mu\text{m}$ silicate absorption from Mason et al. (2006) measured in $0.4''$ steps over a wider region. At and south of the continuum peak the optical depth of the $3.4\ \mu\text{m}$ feature is approximately 0.08, while at the northern locations the depth is noticeably less, approximately 0.06. This pattern is similar to that seen in the silicate feature. The implications of this are discussed in §5.

The $4.5\text{--}5.0\ \mu\text{m}$ portion of the spectrum allows a new search for the presence of the fundamental band of carbon monoxide (CO), which should manifest itself as individual absorption lines if the CO line width is less than the line spacing ($\sim 500\ \text{km s}^{-1}$ or as broad depressions on either side of the band center if the CO line profiles are comparable to or broader than the spacing. Mason et al. (2006), observing at a resolution of $20\ \text{km s}^{-1}$, did not detect narrow CO lines. As discussed earlier CO absorption lines arising in gas orbiting

the AGN outside the characteristic radius of the continuum emitting region should be no wider than 200 km s^{-1} (FWZI).

No signs of absorption by individual lines can be seen in the current spectrum, and any broad depression between the band center and the long wavelength cannot be deeper than about 1% of the continuum. Close examination of the spectrum shows that the continuum in the $4.8\text{--}4.9 \text{ }\mu\text{m}$ portion of the spectrum, corresponding to P branch transitions with $10 < J < 20$, may be depressed by roughly that amount relative to adjacent portions of the spectrum. This could be interpreted as evidence for absorbing CO in dense gas at temperatures of several hundred degrees and with very high velocity dispersion. For an isothermal absorbing slab, lines of CO at this temperature with FWHM's of 500 km s^{-1} and central depths of 1% would produce such a depression and would imply a CO column density of $\sim 1 \times 10^{17} \text{ cm}^{-2}$ and a gas particle density of order 10^7 cm^{-3} . The corresponding portion of the R branch of CO is not available for comparison due to telluric absorption and contamination from the [Ar VI] line. Because the evidence for this broad CO absorption is marginal we regard the above column density as an upper limit.

4. Comparisons and Constraints

4.1. Atomic lines

Both the offsets of the peaks of the [Si IX] and [Al VI] lines from the peak of the continuum and the extents of the line emission are somewhat less than those reported by Marconi et al. (1996) for the coronal lines that they measured along the ionization cone at position angle 31 degrees. However, their measurements were made at roughly five times lower angular resolution than those here. Thus the present determination of the offset should be more accurate. The distributions of the other two coronal lines along the NS slit

are not as well known as those of [Si IX] and [Al VI], but they appear to be similar.

Thompson et al. (2001) imaged the $1.96\ \mu\text{m}$ coronal [Si VI] line at $0.2''$ resolution, finding it to originate mainly to the north-northeast of the the continuum source. The current measurements of the [Si IX] line are largely consistent with Thompson et al. (2001), but failed to detect the fainter line emission that their data show to the south. Prieto et al. (2005) imaged the [Si VII] $2.48\ \mu\text{m}$ line emission at $0.10''$ resolution. Their figures show it to be mostly in a clumpy structure centered on the continuum peak. This appears to differ markedly from the distributions of both the [Si VI] line imaged by Thompson et al. (2001) and the [Si IX] line observed spectroscopically by Marconi et al. (1996) and by us. The accuracy of the co-registration of their images is not available. In the present data the lines and the continuum were measured simultaneously and the result is clear. The ionization energy of [Si VII] lies between those of [Al VI] and [Si IX]; thus it would be surprising if the intensity distribution of the [Si VII] line relative to that of the adjacent continuum were not similar to the lines observed here.

The new measurements of these lines put significant constraints on the size of the high-ionization line emitting region. The detected [Si IX] flux in the UIST slit is about 3.5 times smaller than that reported by Lutz et al. (2000) using the Infrared Space Observatpry (ISO) with a $14'' \times 20''$ aperture, and three times smaller than that reported by Marconi et al. (1996), who used a $4.4''$ slit width. However, assuming that the [Si IX] line-emitting region through which our observations have sliced is roughly circularly symmetric, the total flux in the [Si IX] region is $\sim 5.3 \times 10^{-16}\ \text{W m}^{-2}$, in agreement with the flux measured by ISO and, within the uncertainties, with that by Marconi et al. Using adaptive optics imaging Prieto et al. (2005) fund a rather clumpy distribution of the [Si VII] $2.48\ \mu\text{m}$ line emission extended over $\sim 1''$ but one that does not prefer any particular position angle, so the assumption of circular symmetry, while likely incorrect in detail,

should allow a reasonable estimate of total line flux.

Following the same line of reasoning, the [Al VI] line, which has a very similar flux distribution along the UIST slit as [Si IX] (see Figure 3), would have a total flux of $1.6 \times 10^{-16} \text{ W m}^{-2}$. The total fluxes in the [Ar VI], and [Na VII] lines would be $9 \times 10^{-16} \text{ W m}^{-2}$ and $4 \times 10^{-16} \text{ W m}^{-2}$, respectively. Lutz et al. (2000) found a 1.7 times higher flux for the [Ar VI] line, suggesting that the distribution of this ion, which possesses the lowest ionization energy of the four detected, is somewhat more extended than [Si IX] or possesses a large and very faint halo. Prieto et al. (2005) and Rodríguez-Ardila et al. (2006) found that the [Si VI] and [Si VII] lines (with ionization energies of 167 eV and 205 eV, respectively) each have halos extending to a radius of 70 pc ($1.0''$), but they do not provide the relative contributions of the core and halo.

The absence of hydrogen 5–4 recombination line emission is another noteworthy aspect of the 3–5 μm spectrum in Figure 2. The Br γ line emission detected by Davies et al. (1998) from the circum-nuclear ring of H II regions at a radius of 15–16'' has 1–2 orders of magnitude lower surface brightness than that seen at the nucleus by Tamura et al. (1991). Thus the weakness of the recombination line emission in Figure 2 is not likely to be due to subtraction of bright line emission in the offset beam, located 12'' north of the nucleus, just inside the ring. Davies et al. (2007) have mapped the Br γ line emission in the vicinity of the nucleus at high angular resolution and have kindly made their data available to us. Our limit for the Br α flux in the central $0.2'' \times 1.0''$ of $< 8 \times 10^{-17} \text{ W m}^{-2}$ is 75 times the Br γ line flux in the same aperture. Assuming Case B conditions this limit corresponds to an upper limit on the reddening of 3.5 mag between the wavelengths of the two lines, and, for a $\lambda^{-1.8}$ dependence for the extinction, a visual extinction of no more than ~ 60 mag to the Br γ line-emitting region.

4.2. Solid state and molecular absorptions

The optical depth of the $3.4\ \mu\text{m}$ feature reported here is in good agreement with the values measured by Bridger et al. (1994) and Mason et al. (2004) in larger apertures, but disagrees with values about twice as high reported by Imanishi et al. (1997) and Marco & Brooks (2003). As the bulk of the continuum emission comes from the central point source, the differences with Imanishi et al. (1997) and Marco & Brooks (2003) are difficult to account for in terms of positional variations. In the case of the former paper, incorrect location of the short wavelength continuum may be responsible for the discrepancy, but this does not seem to be the explanation for the Marco & Brooks (2003) result. Neither we, nor any other of the above observers have detected the nuclear $3.3\ \mu\text{m}$ (PAH) emission feature reported by Marco & Brooks (2003). It is possible that some of the features that they see are spurious, perhaps resulting from incorrect cancellation of strong telluric lines present in the $3.25\text{--}3.45\ \mu\text{m}$ interval.

Ayani et al. (1992) and Lutz et al. (2004) searched for lines of the CO fundamental at resolutions of $250\ \text{km s}^{-1}$ and $120\ \text{km s}^{-1}$, respectively. The latter authors set a 3σ upper limit of 7% of the continuum for the depths of individual CO lines. In the $4.57\text{--}4.77\ \mu\text{m}$ portion of the current spectrum, obtained at $150\ \text{km s}^{-1}$ resolution and also devoid of CO lines, the signal-to-noise ratio on the continuum is about three times higher. Thus, the limits both on individual lines separated from one another (i.e., with widths less than $\sim 500\ \text{km s}^{-1}$) and on a broad depression due to blended CO lines are significantly more stringent than those of Lutz et al. (2004).

Finally, Ayani et al. (1992) reported the detection toward the nucleus of NGC 1068 of a narrow absorption feature at $4.69\ \mu\text{m}$, which they attributed to solid CO. Our spectrum shows no such feature, to a limiting absorption depth of a few percent of the continuum.

5. Discussion

5.1. Excitation mechanisms for coronal line emission

One of the most important questions concerning coronal lines in AGN is the excitation mechanism that drives their emission. Here we discuss whether photoionization or shock ionization can account for the locations and strengths of the coronal line emission in NGC 1068. A summary is provided at the end of this section.

5.1.1. Photoionization

Ferguson et al. (1997) carried out a number of illustrative photoionization simulations in an effort to identify the optimal conditions and locations in which the coronal lines form around AGN. Assuming ultraviolet radiation from the central engine as the only excitation mechanism and plane-parallel, constant density slabs of gas, they determined the distances from the ionizing source in which the lines are emitted as a function of density. They provide line equivalent widths in the density-distance plane, indicating where the bulk of the emission occurs for each line, and allowing rough comparisons between observed and predicted emission line flux ratios. The [Al VI], [Ar VI] and [Si IX] lines observed here are included in their calculations. Their figures assume an ionizing ultraviolet continuum similar to that of a typical Seyfert galaxy with $L_{\text{ion}} = 10^{43.5} \text{ erg s}^{-1}$, but distances scale as $L_{\text{ion}}^{1/2}$. Pier et al. (1994) and Bland-Hawthorn et al. (1997) estimate ionizing luminosities 1–2 orders of magnitude higher in NGC 1068.

In the discussion below we assume an ionizing luminosity of $10^{45} \text{ erg s}^{-1}$, which implies locations and dimensions of the emission regions are five times larger than those shown by Ferguson et al. (1997), if all other parameters remain constant. The model then predicts that the distance and density for peak [Si IX] line emission cover 1.5–100 pc

and 10^3 – $10^{6.25}$ cm^{-3} , respectively (with the largest distances corresponding to the lowest densities). The observed distance of 20 pc ($0.3''$) from the nucleus to the peak line emission corresponds to $n \sim 10^4$ cm^{-3}). If the actual peak is closer to the AGN than observed but obscured by dust, then higher density gas would be required.

For the [Al VI] and [Ar VI] lines the adjusted Ferguson et al. (1997) models predict distances to the peak of roughly 15–400 pc for the same density range. Although the spatial distribution of the [Ar VI] line flux is less precise than the other lines, it appears to be similar to that of the other two lines, with a peak at the same location. Clearly the observation that the offset from the AGN to the peaks of these lines of with widely varying excitations are the same is incompatible with an ionized medium of uniform density, unless the extinction is highly non-uniform across the nucleus. The current observations can be roughly reconciled with a slab of density several times 10^4 cm^{-3} if there is increasing extinction of the coronal line emission closer to AGN, of sufficient strength to mask the true peak of the [Si IX] line emission. If the coronal line emission region is symmetrically distributed to the north and south of the AGN, the extinction would need increase further to the south of the AGN in order to block the line emission there from view. Evidence for higher extinction to the south is in fact widespread (e.g., Mason et al. 2006; Das et al. 2006, and references therein). A rough lower limit to the additional extinction required to the south based on the assumption of a symmetric distribution of coronal line emission is two magnitudes at 3.93 μm , which corresponds to approximately 70 visual magnitudes. If the highly non-uniform extinction postulated above is not present, only a density distribution of ionized gas strongly peaked 20 pc north of the AGN could result in photoionization producing the observed maximum line emission from all of these ions at the same location.

The calculations of Ferguson et al. (1997) also indicate that for these ions the regions of significant coronal line emission can extend to much larger distances (~ 100 pc) if gas

densities decrease gradually with distance from the AGN. The near agreement of our estimates of the total flux from the [Si IX] and [Ar VI] lines with measurements made by others in much larger apertures, imply that the ionized gas density must drop steeply at distance greater than ~ 50 pc from the AGN.

5.1.2. *Shock ionization*

Evidence supporting shock ionization in the narrow line regions of AGNs abounds (Marconi et al. 1996; Contini et al. 2002; Prieto et al. 2005; Rodríguez-Ardila et al. 2006). In the case of NGC 1068, Axon et al. (1998) found that $1.5''$ north of the nucleus [Fe VII] is enhanced at the location of the radio jet. They interpreted this as evidence of interaction between the jet and the surrounding medium. The radio jet proceeds outward from the nucleus for an angular distance of several arc-seconds, first nearly due north and then at position angle 35 degrees (Gallimore et al. 1996, 2004). More recently, Das et al. (2006) and Das et al. (2007) have studied the influence of the radio jet on the kinematics of [O III] $\lambda\lambda 4959, 5007$. They observed an increase in the radial velocity roughly proportional to distance from the nucleus followed by a linear decrease beyond ~ 100 pc ($1.4''$) and concluded that the magnitudes of these changes were so large that the neither can the jet be the sole driving force nor can gravity be the sole decelerating mechanism (frictional forces must be significant). However, in the case of that line the deceleration occurs well outside of the region where we observe the higher excitation $3\text{--}5\ \mu\text{m}$ coronal lines.

The line emission reported here originates in ionized regions much closer to the nucleus than those observed by Axon et al. (1998) and Das et al. (2007). Nevertheless, evidence for shock excitation of the coronal lines is also readily apparent when one compares the 5 GHz image in Fig. 1 of Gallimore et al. (2004) with our data. Assuming, as they and Roy et al. (1998) have inferred, that source S1 is coincident with the AGN, and hence with

the infrared continuum peak, the peaks of [Si IX] and [Al VI] line emission at $0.3''$ north are coincident with the bright radio knot C, where the jet bends to the northeast. This is highly suggestive of an interaction between the jet and gas in the NLR. Also suggestive of an interaction at this location is a bright knot of H_2 $2.12\ \mu\text{m}$ line emission found by Müller Sánchez et al. (2009) connecting two streamers of line emission, one of which they interpret as feeding the innermost few parsecs.

The velocity profiles of the [Si IX] line along the spatial direction, shown in Figure 4, also appear to support a jet-NLR interaction. At $0.2''$ north, a prominent blue shoulder is evident in the line profile. That structure also appears to be present $0.4''$ north, but it weakens significantly at $0.6''$. The shoulder at $0.2\text{--}0.4''$ could be associated with ionized gas accelerated toward us by the interaction of the jet with the ambient gas near knot C. The line profile variations are somewhat reminiscent of the behavior of the [Fe VII] $\lambda 6087$ line reported by Rodríguez-Ardila et al. (2006), but the latter is at a much larger distance north of the AGN and, also unlike the infrared lines, far from where that line has its peak intensity.

If shocks are the dominant excitation mechanism for these coronal lines at radio knot C, then it seems likely that some of the remaining [Si IX] and [Al VI] line flux outside of that knot originates in other localized regions and is associated with other radio knots. The knot labeled “NE” in Fig. 1 of Gallimore et al. (2004), located $0.4''$ to the NE of knot “C” and not included in our slit, is a possible candidate for some of this missing line flux. However, judging from the large extent over which [Si VII] was observed by Prieto et al. (2005), we do not think that shocks totally dominate over photoionization, and expect that some contribution of the latter is present, perhaps even at radio knot C.

5.1.3. *Summary*

The infrared coronal line emission peaks 20 pc to the north of the AGN for ions of a wide range of excitation, and extends to 50 pc in the highly excited [Si IX] line and presumably at least as far in the other lines. To the south there is no clear detection of any of the 3–5 μm lines. Increased extinction to the south can account for the north-south asymmetry, regardless of the line excitation mechanism. However, photoionization by the AGN producing peaks at equal northern distances from the AGN for such a large range of excitations requires a highly asymmetric gas distribution and/or a highly asymmetric distribution of obscuring dust to the north. This explanation appears contrived. Evidence for collisional excitation of these lines is more compelling; it consists of the spatial coincidence between radio knot C (where the jet changes direction), a prominent knot of H_2 line emission, and the emission peaks of all of the 3–5 μm coronal lines. The presence at the same location of a localized prominent high velocity blue-shifted shoulder on the [Si IX] line provides further support. Higher angular resolution studies of the coronal line emission would allow a more detailed comparison with the morphology of the radio emission.

5.2. **The 3.4 μm absorption feature and the non-detection of CO**

In this subsection we discuss that portion of the interstellar medium producing the hydrocarbon and silicate absorption features at 3.4 μm and 9.7 μm , but little or no absorption by gaseous CO at 4.5–5.0 μm . Our discussion makes use of the silicate absorption feature as reported by Mason et al. (2006); its similar behavior across the nucleus as the 3.4 μm feature provides a strong clue as to the nature of the interstellar medium. The subsection on CO examines a number of possible explanations for its absence, and results in a similar conclusion regarding the ISM. A summary is provided at the end of this section.

It is important to note that in the direction along the (NS) slit the continuum source was partially resolved at UKIRT and therefore we are assured that it has a characteristic dimension of a few tens of parsecs. Thus the bulk of the material producing the $3.4\ \mu\text{m}$ absorption feature and not producing CO absorption lies 10 pc or more from the central engine. Dust and gas in the central few parsecs can only be a minor contributor to the present spectrum and our arguments as to the nature of the interstellar medium therefore apply to the more extended region and not to the “core” or the innermost region of the torus observed via interferometry.

5.2.1. *The $3.4\ \mu\text{m}$ band*

The spectral profile of the $3.4\ \mu\text{m}$ feature is well characterized in the current data. Overall the profile is smooth, showing only the two principal sub-features seen in Galactic sources, those at $3.420\ \mu\text{m}$ and $3.485\ \mu\text{m}$. The profile in NGC 1068 contains no evidence of a distinct $3.385\ \mu\text{m}$ sub-feature, which is sometimes present in Galactic sources and sometimes blended with the $3.420\ \mu\text{m}$ feature (Pendleton et al. 1994; Chiar et al. 2002).

The data also reveal that the depth of the $3.4\ \mu\text{m}$ feature has a similar north-south variation across the nucleus as the $9.7\ \mu\text{m}$ silicate absorption (Fig. 5). Both features are at maximum depth on and just to the south of the nucleus. The similarity is also quantitative; the fractional increase in the depth of each feature at its maximum compared to the depth at adjacent locations is ~ 40 percent. *This indicates that the carriers of the features are significantly mixed.* The compactness and nuclear location of the region of enhanced $3.4\ \mu\text{m}$ and silicate extinction suggests that the extra absorption to the south occurs quite close to the nucleus. In the silicate feature the weaker off-nuclear absorption extends over $2''$ to the north and south. Because the $3\ \mu\text{m}$ continuum source is much more compact, the depth of the $3.4\ \mu\text{m}$ feature could not be measured more than $0.4''$ distant from the nucleus. The

lower level and more extended silicate feature largely arises in a circumnuclear region of much larger dimensions than the torus-like structures seen with mid-IR interferometry. It may be associated with material in the disk of the host galaxy, which crosses the line of sight south of the nucleus. The distinction between these two regions is not necessarily sharp (Packham et al. 2007).

The ratio of the optical depths of the $3.4\ \mu\text{m}$ and silicate features at the infrared continuum peak of NGC 1068 is 0.19 ± 0.02 . In the Galaxy the silicate feature is found in both diffuse and dense interstellar clouds, whereas the hydrocarbon feature is found only in diffuse clouds. In diffuse clouds far from the Galactic center the ratio of optical depths of the two features can be derived from their optical depths relative to A_V , $A_V/\tau_{9.7} \approx 18.5$ (Roche & Aitken 1984) and $A_V/\tau_{3.42} \approx 250$ (Pendleton et al. 1994), yielding $\tau_{3.4}/\tau_{9.7} = 0.07 \pm 0.01$, a value roughly forty percent of that measured in NGC 1068. Toward the Galactic center, where $A_V \approx 30$ mag), the value of $\tau_{3.4}/\tau_{9.7}$ averaged over sources observed by both Chiar et al. (2002) and Roche & Aitken (1985) is 0.064 ± 0.017 , the same as the above value to within the uncertainties. The ratio *in just the diffuse gas on the Galactic center sightline* may be estimated as follows. Pendleton et al. (1994) find $A_V/\tau_{3.4} = 156 \pm 16$ and Roche & Aitken (1985) find $\tau_{9.7} = 3.6 \pm 0.3$. However, one-third of the visual extinction to the Galactic center is believed to occur in dense clouds, located mostly in intervening spiral arms (Whittet et al. 1997). Following Chiar et al. (2007), for values of $A_V < 12$ mag the ratio of visual extinction to silicate optical depth is the same in dense clouds as in diffuse clouds, and thus we associate those 10 mag of dense cloud visual extinction with a silicate optical depth of 0.54. This gives $\tau_{3.4}/\tau_{9.7} \approx 0.23/3.06 = 0.075$ for Galactic center diffuse clouds, again far less than the ratio toward the nucleus of NGC 1068. Even if half of the silicate optical depth toward the Galactic center arises in the dense clouds in the Galactic disk, the above ratio would only be 0.15, less than the value in NGC 1068.

Clearly then, the $3.4\ \mu\text{m}$ absorption in NGC 1068 is unusually strong relative to the silicate absorption. This cannot be explained away by placing the $3.4\ \mu\text{m}$ absorber in a more remote location than the silicate feature, because even in Galactic diffuse clouds the optical depth of 0.08 observed in NGC 1068, corresponds to a silicate optical depth $\gtrsim 1$, significantly larger than is observed. The high ratio could be the result of the silicate absorption being significantly filled in, as might arise if thermal emission close to the AGN were absorbed in the cooler outer portions of the source. Because such filling in would be much less for the $3.4\ \mu\text{m}$ feature, the similar variation in optical depths of the features across the nucleus tends to argue that this is not the entire explanation, however. As suggested by Imanishi (2000), the high ratio could be explained, at least in part, by the typical continuum surface at $3.4\ \mu\text{m}$ lying interior to the typical surface at $9.7\ \mu\text{m}$ such that the added pathlength, unobservable at $9.7\ \mu\text{m}$, contains a significant fraction of the observed column density of the $3.4\ \mu\text{m}$ absorber. The result also could be a consequence of either unusual elemental abundances or the chemistry of the dust in the vicinity of the AGN.

5.2.2. *The non-detection of CO*

The CO fundamental band has been searched for previously without success in NGC 1068 at spectral resolutions ranging from $20\ \text{km s}^{-1}$ to $250\ \text{km s}^{-1}$ (Ayani et al. 1992; Lutz et al. 2004; Mason et al. 2006). The current data, obtained at $150\ \text{km s}^{-1}$ resolution, significantly tightens the limit on absorption by CO in the warm and presumably rapidly moving gas just outside of the $3\text{--}5\ \mu\text{m}$ continuum-emitting dust, whose FWHM along the ionization cones is $\sim 20\ \text{pc}$. In its lack of detectable CO in this band NGC 1068 is similar to the five other Type 2 Seyferts studied by Lutz et al. (2004), although the limits on CO absorption in those galaxies are considerably less strict.

We consider three possible explanations for the lack of strong CO absorption lines toward the AGN in NGC 1068: (1) the molecules are distributed among many rotational states; (2) the molecules reside in a clumpy obscuring medium; and (3) there is a paucity of “dense cloud” molecular gas in front of the AGN. To explain the non-detection of transitions of CO, OH and H₂CO lines from low rotational levels towards the highly obscured nucleus of Cygnus A at radio wavelengths, it has been pointed out that at the temperatures of the nuclear clouds the lowest rotational levels may contain only a small fraction of the molecules (Barvainis & Antonucci 1994; Maloney et al. 1994; Conway & Blanco 1995). For example, in LTE at 300 K roughly twenty rotational levels of CO have populations within a factor of ten of that of the most populated level, whereas at 25 K only the six lowest levels are so highly populated. It also has been suggested by these authors that under some circumstances a strong and compact nuclear radio source could redistribute the rotational level populations in the surrounding gas, further weakening the strengths of lines from the low rotational levels. Impellizzeri et al. (2006) find this explanation unlikely, however, because the 19% of their sources in which high-excitation OH lines are detected also show absorption from the ground state transition.

In the case of NGC 1068, whose 3–5 μ m continuum-emitting dust, and presumably the gas associated with this dust, are at temperatures of several hundred Kelvins, the LTE fractional populations in the low lying levels normally observed at radio and millimeter wavelengths would be much less than in galactic dense clouds. This cannot be the explanation for the non-detection of the CO fundamental band lines, however, as the *M* band spectrum in Fig. 2 encompasses lines with a wide range of lower state energies (corresponding to $J = 1$ –30 in the case of the P branch).

The second possibility is that, although there is a large amount of molecular material along the line of sight to the nuclear continuum source, it is concentrated into clumps that

cover only a small fraction of the source. Each individual clump produces deep CO lines but as most of the continuum source is unobscured, the net effect is much weaker CO absorption. Such small cloud volume filling factors have been invoked in order to explain the mid-infrared observational properties of Seyfert 1 and Seyfert 2 galaxies in the unified model (in particular the lack of silicate emission in the former and the broad spectral range of the far-infrared continuum; Nenkova et al. 2002). Small filling factors for toroids surrounding AGNs are also predicted by the hydrodynamic simulations of Wada (2007).

If the detectability of CO absorption is related to the cloud filling factor, then for similar total extinction CO should be detected in objects with smooth obscuration (i.e., covering the entire nuclear continuum source), but not in those with clumpy obscuration. Sirocky et al. (2008) propose that clumpy and smooth obscuration in AGN can be separated on the basis of the strength of the 10 and 18 μm silicate features. Strong CO absorption, in gas that is warm and presumably close to the nuclear source, has been detected in several AGN-hosting ultraluminous infrared galaxies (ULIRGs) (Spoon et al. 2004; Geballe et al. 2006; Shirahata et al. 2007; Sani et al. 2008), whose silicate features would classify their dust distribution as smooth, whereas in the single Seyfert 2 ULIRG whose spectrum would classify it as clumpy, only a weak CO band has been tentatively detected (Sani et al. 2008). This may suggest that the strength of the molecular absorption in AGN is indeed governed by the clumpiness of the obscuring medium, but a stringent test of this hypothesis will require a larger sample of objects spanning a wide range of dust geometries.

Nevertheless, the presence in NGC 1068 of the 3.4 μm feature, whose spatial behavior suggests that much of it arises in the same gas as much of the silicate feature, close to the AGN, raises immediate complications with the clumpy model. That model has the dust and gas local to the AGN residing in dense clouds with a small filling factor, so that the silicate absorption, which is strong in each clump, is both diluted and filled in by emission

(Nenkova et al. 2002). The CO absorption lines would also be diluted by this arrangement, apparently to undetectability in the case of NGC 1068. However, the absence of the $3.4\ \mu\text{m}$ band in Galactic dense molecular clouds suggests that in NGC 1068 the carrier of that band would not reside in such clumps, and thus that a second, more diffuse medium is needed for it (ignoring, for the moment the evidence that the carriers of the two dust features are mixed). The diffuse material could, for example, be a low-density interclump medium. However, the $3.4\ \mu\text{m}$ band in Galactic diffuse clouds is invariably accompanied by a silicate absorption feature. As pointed out earlier, the previously estimated value of $\tau_{3.4}/\tau_{9.7}$ in the diffuse interstellar medium toward the Galactic center, when applied to NGC 1068, implies that most or all of silicate absorption in NGC 1068 must arise in that material carrying the $3.4\ \mu\text{m}$ band.

The by now almost inevitable solution to these problems is the third explanation: at $3\text{--}13\ \mu\text{m}$ essentially all of the absorbing material in the line of sight has the chemical characteristics of Galactic diffuse clouds. In this explanation clumpy absorbing material is not needed to account for the lack of detectable CO, because in diffuse clouds CO is mostly dissociated, comprising only one percent of the carbon. Diffuse clouds do have large molecular components, with H_2 accounting for typically half of the hydrogen; thus H_2 should be available to provide the line emission observed by Müller Sánchez et al. (2009). The dust grains in diffuse clouds are comprised of a refractory component responsible for the $3.4\ \mu\text{m}$ feature and a silicate component. Gas densities in Galactic diffuse clouds are $10\text{--}1000\ \text{cm}^{-3}$. Densities in the inner few tens of parsecs of NGC 1068 might be greater than this. However, at distances of only a few tens of parsecs from a luminous AGN it may well be possible that somewhat denser gas also has the above characteristics.

As discussed earlier, in the Galaxy fairly tight relationships have been found between the visual extinction in the diffuse ISM and the depth of the $3.4\ \mu\text{m}$ feature (Pendleton et al.

1994) for sightlines to the Galactic center and to local diffuse clouds. Here we employ the former relationship, $A_V/\tau_{3.4} = 150$. Using it we estimate a typical visual extinction of 12 mag to the $3.4\ \mu\text{m}$ continuum-emitting region, implying for a normal gas-to-dust ratio that $N(\text{H}) = 2.3 \times 10^{22}\ \text{cm}^{-2}$. Then, assuming that, as in Galactic diffuse clouds, one percent of the carbon is in CO, and also (conservatively) that the typical continuum surface at $3.4\ \mu\text{m}$ and $4.7\ \mu\text{m}$ are at the same depth, $N(\text{CO}) = 6 \times 10^{16}\ \text{cm}^{-2}$, which is consistent with the upper limit of $1 \times 10^{17}\ \text{cm}^{-2}$ set by these observations. The above column density of hydrogen is much less than the column density that attenuates our view of the central engine, $N(\text{H}) > 10^{25}\ \text{cm}^{-2}$ (Matt et al. 2004), but much of that gas must be interior to the dust that is emitting the observed $3\text{--}5\ \mu\text{m}$ continuum.

5.2.3. Summary

We have found that the $3.4\ \mu\text{m}$ hydrocarbon and $9.7\ \mu\text{m}$ silicate bands have spatial variations that are similar across the central 0.2×0.8 arcsecond of NGC 1068 and that only a small fraction of interstellar carbon in this region can be in the form of CO. The first finding indicates that the carriers of the $3.4\ \mu\text{m}$ and $9.7\ \mu\text{m}$ bands are largely mixed and that significant fractions of each are located in material very close to the nucleus. In the Galaxy both features are present in diffuse interstellar clouds, but the $3.4\ \mu\text{m}$ band is *only* observed there. The fraction of CO in diffuse clouds is small and our observed upper limit in NGC 1068 is consistent with such a location. Measurable CO absorption would be present if even a modest fraction of the silicate absorption arose in fully molecular material. The straightforward conclusion is that *the 3-13 μm absorption spectrum of NGC 1068 is produced in material chemically similar to the Galactic diffuse interstellar medium.*

We reiterate the significance of the lack of detection of CO and its incompatibility with models employing clumps of *dense molecular* material, even if such material near an AGN is

capable of producing the $3.4\ \mu\text{m}$ feature. If the filling factor of such fully molecular clumps were low enough to “dilute” the CO band to non-detection, as observed, similar dilutions would occur for the silicate and $3.4\ \mu\text{m}$ absorptions, contradicting the observations.

The adaptive optics measurements of Gratadour et al. (2006) show that nuclear thermal infrared continuum arises in part from numerous clumps covering a few tens of parsecs. If the source of the $3\text{--}13\ \mu\text{m}$ continuum is dominated by such clumps, then absorbing material could either be located on surfaces of the clumps or be more continuously distributed in front of them. However, if a significant portion of the continuum is emitted by an extended component, the present observations constrain the degree of clumpiness in the absorbing material. In that case a low, e.g. <0.1 , filling factor for the absorbing clumps probably would be inconsistent with the observed strength of the $3.4\ \mu\text{m}$ feature, as it would imply, e.g., $\tau(3.4\ \mu\text{m}) > 0.8$ in the clumps. The maximum observed optical depth of the feature is 0.5, in the deeply buried ULIRG IRAS 08572+3915 (Geballe et al. 2006).

6. Conclusions

The observations reported here bear largely on two important issues: (1) the ionization mechanism for the high excitation coronal line emission close to the AGN; and (2) the nature of the dusty environment absorbing the infrared continuum of the AGN. Regarding the ionized gas, the evidence appears to both favor collisional excitation of the bulk of the coronal line emission and, in view of the spatial coincidences of the various lines, argue against photoionization. Regarding the absorbing material, the simplest explanation is that it has much more of the characteristics of diffuse clouds than dense clouds (clumped or unclumped). The strength of the hydrocarbon feature argues against it being distributed in front of the sources of the continuum with a very low filling factor relative to them. Because elsewhere it has always been found that silicate dust is always present where a

3.4 μm absorption is observed, one can conclude that if the latter is not so distributed then neither is the former.

Finally, it should be noted that in NGC 1068 the extended source of the 3–5 μm continuum radiation has a characteristic north-south dimension of ~ 20 pc, indicating that the bulk of the continuum emission occurs at distances of ~ 10 pc or more from the central engine. This distance is much greater than that estimated under the assumption that the temperature of the dust is determined principally by the luminosity of the AGN and its distance. Using an AGN luminosity of $1.5 \times 10^{11} L_{\odot}$ (Weinberger et al. 1999), dust grains heated by isotropic radiation from the AGN to the observed 3–5 μm color temperatures of ~ 500 K would lie only ~ 1 pc from the AGN. Gratadour et al. (2006) has suggested that transient heating of small grains could be responsible for the high temperatures. We speculate that at least in the north-south direction mechanical heating of the dust and gas, perhaps from the AGN jets, could also be important.

We thank the staff of the United Kingdom Infrared Telescope, which is operated by the Joint Astronomy Centre on behalf of the Science and Technology Facilities Council of the U.K. TRG’s and REM’s research is supported by the Gemini Observatory, which is operated by the Association of Universities for Research in Astronomy, Inc., under a cooperative agreement with the NSF on behalf of the Gemini partnership: the National Science Foundation (United States), the Science and Technology Facilities Council (United Kingdom), the National Research Council (Canada), CONICYT (Chile), the Australian Research Council (Australia), Ministério da Ciência e Tecnologia (Brazil) and SECYT (Argentina). ARA’s research was partially supported by the Brazilian funding agency CNPq (311476/2006-6). We are grateful to N. A. Levenson for useful discussions and to the anonymous referee for numerous helpful comments.

REFERENCES

- Axon, D. J., Marconi, A., Capetti, A., Maccetto, F. D., Schreier, E., & Robinson, A. 1998, *ApJ*, 496, L75
- Ayani, K., Nakagawa, T., & Nagata, T. 1992, in "Testing the AGN paradigm; Proceedings of the 2nd Annual Topical Astrophysics Conference," ed. S. Holt, S. Neff, & C. M. Ury, AIP Conference Proceedings, 254, 528.
- Barvainis, R. & Antonucci, R. 1994, *AJ*, 107, 1291
- Bian, W. & Gu, Q. 2007, *ApJ*, 657, 159
- Bland-Hawthorn, J., Lumsden, S. L., Voit, G. M., Cecil, G. N., & Weisheit, J. C. 1997, *ApSS*, 248, 177
- Bohlin, R. C., Savage, B. D., Drake, J. F. 1978, *ApJ*, 224, 132
- Bridger, A., Wright, G. S., & Geballe, T. R. 1994, in "Infrared Spectroscopy With Arrays: The Next Generation," ed. I.S. McLean, Kluwer (Dordrecht), 537-538
- Capetti, A., Macchetto, F. D., & Lattanzi, M. G. 1997, *ApSS*, 248, 245
- Chiar, J. E., Adamson, A. J., Pendleton, Y. J., Whittet, D. C. B., Caldwell, D. A., & Gibb, E. L. 2002, *ApJ*, 570, 198
- Chiar, J. E., et al. 2007, *ApJ*, 666, L73
- Contini, M., Viegas, S.M., & Prieto, M. A. 2002, *A&A*, 386, 399
- Conway, J. E. & Blanco, P. R. 1995, *ApJ*, 449, L131
- Dartois, E., Marco, O., Muñoz-Caro, G. M., Brooks, K., Deboffle, D., d'Hendecourt, L. 2004, *A&A*, 423, 549

- Das, V., Crenshaw, D. M., Kraemer, S. B., & Deo, R. P. 2006, *ApJ*, 132, 620
- Das, V., Crenshaw, D. M., & Kraemer, S. B. 2007, *ApJ*, 656, 699
- Davies, R. I., Sugai, H., & Ward, M. J. 1998, *MNRAS*, 300, 388
- Davies, R. I., Mueller Sánchez, F., Genzel, R., Tacconi, L. J., Hicks, E. K. S., Friedrich, S., & Sternberg, A. 2007, *ApJ*, 671, 1388
- Ferguson, J. W., Korista, K. T., Baldwin, J. A., & Ferland, G. J. 1997, *ApJ*, 487, 122
- Gallimore, J. F., Baum, S. A., O’Dea, C. P., & Pedlar, A. 1996, *ApJ*, 458, L36
- Gallimore, J. F., Baum, S. A., & O’Dea, C. 2004, *ApJ*, 613, 794
- Geballe, T. R., Goto, M., Usuda, T., Oka, T., & McCall, B. J. 2006, *ApJ*, 644, 907
- Geballe, T. R., McCall, B. J., Hinkle, K., & Oka, T. 1999, *ApJ*, 510, 251
- Gebhardt, K., et al. 2000, *ApJ*, 539, L13
- Gratadour, D., Rouan, D., Mugnier, L. M., Fusco, T., Clénet, Y., Gendron, E., & Lacombe, F. 2006, *A&A*, 446, 813
- Hönig, S. F. & Beckert, T. 2007, *MNRAS*, 380, 1172
- Hönig, S. F., Prieto, M. A., & Beckert, T. 2008, *A&A*, 485, 33
- Imanishi, M., Terada, H., Sugiyama, K., Motohara, K., Goto, M., & Maihara, T. 1997, *PASJ*, 49, 69
- Imanishi, M. 2000, *MNRAS*, 319, 331
- Impellizzeri, V., Roy, A. L., & Henkel, C. 2006, *Proc. of Sci*, 8th Eur. VLBI Network Symp., ed. A. Marecki, 35

- Jaffe, W., et al. 2004, *Nature*, 429, 6987
- Krolik, J. H. & Begelman, M. C. 1986, *ApJ*, 308, L55
- Krolik, J. H. & Begelman, M. C. 1988, *ApJ*, 329, 702
- Lee, H.-H., Bettens, R. P. A., & Herbst, E. 1996, *A&AS*, 119, 111
- Lutz, D., Sturm, E., Genzel, R., Moorwood, A. F. M., Alexander, T., Netzer, H., & Sternberg, A. 2000, *ApJ*, 536, 697
- Lutz, D., Sturm, E., Genzel, R., Spoon, H. W. W., & Stacey, G. J. 2004, *A&A*, 426, L5
- Macchetto, F., Capetti, A., Sparks, W. B., Axon, D. J., & Boksenberg, A. 1994, *ApJ*, 435, L15
- Maloney, P. R., Begelman, M. C., & Rees, M. J. 1994, *ApJ*, 432, 606
- Marco, O. & Alloin, D. 2000, *A&A*, 353, 465
- Marco, O., & Brooks, K. J. 2003, *A&A*, 398, 101
- Marconi, A., van der Werf, P. P., Moorwood, A. F. M., & Oliva, E. 1996, *A&A*, 315, 335
- Mason, R. E., Wright, G., Pendleton, Y., & Adamson, A. 2004, *ApJ*, 613, 770
- Mason, R. E., Geballe, T. R., Packham, C., Levenson, N. A., Elitzur, M., Fisher, R. S., & Perlman, E. 2006, *ApJ*, 640, 612
- Mason, R. E., Wright, G. S., Adamson, A., & Pendleton, Y. 2007, *ApJ*, 656, 798
- Matt, G., Bianchi, S., Guainazzi, M., & Molendi, S. 2004, *A&A*, 414, 155
- Müller Sánchez, F., Davies, R. I., Genzel, R., Tacconi, L. J., Eisenhauer, F., Hicks, E. K. S., Friedrich, S., & Sternberg, A. 2009, *ApJ*, 691, 749

- Muxlow, T. W. B., Pedlar, A., Holloway, A. J., Gallimore, J. F., & Antonucci, R. R. J. 1996, MNRAS, 278, 854
- Nenkova, M., Ivezić, Z., & Elitzur, M. 2002, ApJ, 570, L9
- Packham, C., Radomski, J. T., Roche, P. F., Aitken, D. K., Perlman, E., Alonso-Herrero, A., Colina, L., & Telesco, C. M. 2005, ApJ, 618, L17
- Packham, C., et al. 2007, ApJ, 661, L29
- Pendleton, Y. J., Sandford, S. A., Allamandola, L. J., Tielens, A. G. G. M., & Sellgren, K. 1994, ApJ, 437, 683
- Pier, E/ A/, Antonucci, R., Hurt, T., Kriss, G., & Krolik, J. 1994, ApJ, 428, 124
- Poncelet, A. & Perrin, G., & Sol, H. 2006, A&A, 450, 483
- Prieto, M. A., Marco, O., & Gallimore, J. 2005, MNRAS, 364, L28
- Raban, D., Jaffe, W., Röttgering, H., Meisenheimer, K., & Tristram, K. R. W. 2009, MNRAS, 394, 1325
- Ramsay Howat, S., et al. 2004, Proc. SPIE, 5492, 1160
- Rhee, J. H. & Larkin J. E. 2006, ApJ, 640, 625
- Roche, P. F. & Aitken, D. A. 1984, MNRAS, 208, 481
- Roche, P. F. & Aitken, D. K. 1985, MNRAS, 215, 425
- Roche, P. F., Packham, C., Telesco, C. M., Radomski, J. T., Alonso-Herrero, A., Aitken, D. A., Colina, L., & Perlman, E. 2006, MNRAS, 367, 1689
- Roche, P. F., Packham, C., Aitken, D. K., & Mason, R. E. 2007, MNRAS, 375, 99

- Rodríguez-Ardila, A., Prieto, M. A., Viegas, F.S., & Gruenwald, R. 2006, *ApJ*, 653, 1098
- Roy, A. L., Colbert, E. J. M., Wilson, A. S., & Ulvestad, J. S. 1998, *ApJ*, 504, 147
- Sandford, S. A., Allamandola, L. A., Tielens, A. G. G. M., Sellgren, K., Tapia, M., & Pendleton, Y. 1991, *ApJ*, 371, 607
- Sani, E. 2008, *ApJ*, 675, 96
- Shirahata, M., Nakagawa, T., Goto, M., Usuda, T., Suto, H., & Geballe, T.R. 2006, in "The Central Engines of Active Galactic Nuclei," L. C. Ho & J.-M. Wang eds., A. S. P. Conf Ser., 373, 505
- Sirocky, M. M., Levenson, N. A., Elitzur, M., Spoon, H. W. W., & Armus, L. 2008, *pJ*, 678, 729
- Spoon, H. W. W., et al. 2004, *ApJS*, 154, 184
- Tamura, M., Kleinmann, S. G., Scoville, N. Z., & Joyce, R. R. 1991, *ApJ*, 371, 131
- Thompson, R. I., Chary, R.-R., Corbin, M. R., & Epps, H. 2001, *ApJ*, 558, L97
- Tristram, K. R. W., et al. 2007, *A&A*, 474, 837
- Tully, R. B. 1988, *Nearby Galaxies Catalog* (Cambridge: Cambridge Univ. Press)
- Wada, K. 2007, *PASJ*, 59, 711
- Weinberger, A. J., Neugebauer, G., & Mathews, K. 1999, *AJ*, 117, 2748
- Whittet, D. C. B., et al. 1997, *ApJ*, 490, 729
- Young, S., Packham, C., Mason, R. E., Radomski, J. T., & Telesco, C. M. 2007, *MNRAS*, 378, 888

